scientific reports

Check for updates

OPEN

Machine learning enhanced design and knowledge discovery for multi-junction photonic power converters

Robert F. H. Hunter[1]✉, Gavin P. Forcade[1], Yuri Grinberg[2], D. Paige Wilson[1], Meghan N. Beattie[1], Christopher E. Valdivia[1], Mathieu de Lafontaine[1], Louis-Philippe St-Arnaud[1], Henning Helmers[3], Oliver Höhn[3,4], David Lackner[3], Carmine Pellegrino[3], Jacob J. Krich[1], Alexandre W. Walker[5] & Karin Hinzer[1]

Machine learning is proving to be a revolutionary tool across many disciplines, including optoelectronic device design. In this report, we compare classical and machine learning enhanced design optimization methodologies. We investigate, as an example case, the design of the complex structures of ten-junction InP lattice matched photonic power converters with $In_{0.53}Ga_{0.47}As$ absorbers optimized for operation at 1550 nm. We find that the implicit pattern recognition capabilities of dimensionality reduction using principal component analysis accelerate design discovery, optimization, and the understanding of complex optical phenomena in the simulated devices. The dimensionality reduction approach offers over twenty times as many optimal designs with greater variability and with a 15% reduction in computational cost compared to a classical optimization method. Furthermore, we find that the representation of the reduced dimensionality subspace offers an intuitive interpretation of optical phenomena expected to occur in this design problem. This method is general and offers the potential for knowledge discovery, expanded design perspective, and optimization acceleration in conjunction with a significant reduction in computational expense in systems which can be numerically modeled.

Keywords Machine learning, Dimensionality reduction, Design discovery, Optimization acceleration, Knowledge discovery, Multi-junction photonic power converters

Optoelectronic device design relies upon the expertise of the design team to guide the process towards a desired outcome. However, the complexity of many devices quickly makes this process intractable as the number of parameters to consider is large and their correlations non-trivial. Classical optimization strategies, such as brute-force[1–3], genetic[2,3], or multi-objective optimization algorithms[4], are employed but come with several drawbacks[5]. First, their large computational expense scales with the number of varied parameters in the design space, exponentially in the worst cases. Second, there is no guarantee of finding an adequate solution since they are sensitive to the designer's initial assumptions and to the complexity of the input-output relation. And third, they cannot efficiently handle multi-objective problems, which is standard for most optoelectronic applications. Contemporary tools based on machine learning (ML) algorithms offer a way forward in these complex design problems, expanding the design perspective by reducing computational load and dependence upon the design team's input while simultaneously bolstering the understanding of the physics underlying the problem.

Supervised learning and dimensionality reduction are two common machine learning strategies for optoelectronic design. Supervised learning methods typically employ neural networks, which reduce computational cost by learning the input-output relation. This contributes to the great success of neural network based approaches in the inverse design problem, where the device design is obtained from the desired response[2,3,6–11]. However, these methods are; 1) not interpretable, 2) do not reliably represent the many-to-one problem, where many sets of design parameters produce the same output response, which includes the design of many optoelectronic devices[9,12], and, 3) in the case of high-dimensional spaces, may still require computationally expensive data collection efforts to train. On the other hand, dimensionality reduction is a machine learning

[1]SUNLAB, Nexus for Quantum Technologies Institute, University of Ottawa, Ottawa, ON, Canada. [2]Digital Technologies Research Centre, National Research Council of Canada, Ottawa, ON, Canada. [3]Fraunhofer Institute for Solar Energy Systems ISE, Freiburg 79110, Germany. [4]Department of Sustainable Systems Engineering (INATECH), University of Freiburg, Freiburg 79110, Germany. [5]Quantum and Nanotechnologies Research Centre, National Research Council of Canada, Ottawa, ON, Canada. ✉email: rhunt013@uottawa.ca

method to significantly reduce the computational cost of optimization while simultaneously identifying and encapsulating relationships in the data, enabling knowledge discovery. It operates to find the most compact representation of high-dimensional data with minimal information loss, greatly reducing the complexity of the problem. The reduced dimensional space offers fertile ground for efficient optimizations or multi-objective parameter sweeps[12–22]. The construction of the reduced dimensional space provides insights to supplement the design team's understanding of the device and design landscape. This expansion in design perspective may speed up, improve, or lead to entirely new paradigms in the device design[12,17,23–25].

In this work, we extend the dimensionality reduction based method of Melati et al. [13]. We compare this machine learning (ML) enhanced method to a classical optimization strategy and the conventional "Beer-Lambert" approach for the chosen example design problem: multi-junction photonic power converters (PPCs). We study the nature of the optimized devices and explain the systematic deviations away from the typical approach that are observed. Comparing optimizations, we find that the ML-enhanced method offers over twenty times as many top designs with greater variability and at lower computational cost than the classical optimization approach. Ultimately, we identify that the top optimized designs from both methods and the Beer-Lambert design have comparable optoelectronic power conversion efficiencies (due to luminescent coupling and high material quality). Nonetheless, the variety of high-performance designs discovered, especially in the ML approach, is advantageous to applications where multiple figures of merit (FOM) are considered, as is often the case in reality. We further examine the construction of the reduced dimensional space and link features of the dimensionality reduction to the physical phenomenology of the design space. To the best of our knowledge, this is the first application of machine learning to the design of photonic power converters. It also constitutes an in-depth examination of dimensionality reduction based design for knowledge discovery following the examples of Melati et al. [16] and Kiarashinejad et al. [12,23–25].

Multi-junction photonic power converter design optimization

Background and conventional design approach

Photonic power converters (PPCs) are photovoltaic devices optimized to convert laser light into electrical power. They are part of the receiver unit in power-by-light systems and some optical-wavelength telecommunications links, with many modern applications in 5G, internet-of-things, remote power, and more[26–44]. Vertically-stacked monolithic multi-junction device architectures with several p-n junctions connected in series using tunnel diodes are state-of-the-art. They enable operation under higher optical power densities than other architectures and, thus, enable the highest electrical output powers. Simultaneously, their increased voltage output negates the need for step-up voltage converters on the remote side improving system efficiency[27,45–50]. When compared to single-junction designs, they allow lower current densities, reducing series resistance losses, and have thinner junctions that loosen material diffusion length constraints and reduce bulk recombination losses[27,50–54]. Multi-junction devices have achieved record efficiencies above 65% (GaAs absorbers, 5-junction, ~830-840 nm, ~1.25 W input power, at 25°C[55]) and output powers in excess of 29 W (GaAs absorbers, 12-junction, ~810 nm, efficiency of ~61%[56]). PPCs with 30 junctions are commercially available[50]. In this work, we consider ten-junction (10J) PPCs with an absorber material of $In_{0.53}Ga_{0.47}As$ lattice matched to an InP substrate, hereafter referred to as InGaAs. The InGaAs absorber material (bandgap $\approx$ 0.736 eV) has been chosen for system operation at a laser wavelength of ~1550 nm, which benefits from the advantageous free space and fibre optic transmission properties at this wavelength[27,28,48,57,58]. We choose ten junctions to allow output voltages greater than 5 V as desirable for powering downstream electronics. This junction multiplicity matches the state-of-the-art devices in this material system[45].

The simplest design approach to vertically stacked multi-junction PPCs employs the Beer-Lambert law to calculate the absorber layer thicknesses. This law stipulates that the optical power decreases exponentially as a function of depth into a semiconductor material. Due to the current matching constraints of series-connected junctions, Beer-Lambert designs have junctions which increase in thickness from the light-incident side down (see Fig. 1). This serves as a reasonable first-order estimate and has been used to achieve high device performance[45]. In its simplest application, the Beer-Lambert method does not account for auxiliary non-absorbing layers, optical effects such as interference, interfaces, doping, and parasitic absorption. Additional to the absorber layers, PPCs employ anti-reflection coatings (ARCs), top-side dielectric layers which help couple light into the device. The thicknesses of the ARC layers are often designed by maximizing the transmission into a simple material stack with a uniform refractive index, neglecting the optical coupling of these layers to the full device structure. In this paper, we consider Beer-Lambert absorber designs with double-layer ARCs optimized using simple structures and those optimized using the full active stack, and compare these designs to the top results from the optimization methods. We ascertain that the approximations implicit in these conventional approaches do not significantly affect the optoelectronic power conversion efficiency for our 10J device. We attribute this to the weak optical coupling present in the structure and to luminescent coupling. Beer-Lambert designs are specified in the text by the fraction of incident light absorbed in the full device.

Device model and calibration

We evaluate devices using an accurate and predictive one-dimensional Poisson/drift-diffusion device model built in Synopsys Sentaurus TCAD[59]. We simulate optical absorption, including interference effects in layers thinner than the wavelength of incident light, using a rigorous coupled wave analysis (RCWA) optical solver, S4[60,61]. For computational efficiency, we implement scikit-learn[62] optimization capabilities directly in the S4 python interface to Sentaurus. We assume standard one-to-one conversion of absorbed photons to electron-hole pairs and couple the resulting optical carrier generation rates from the RCWA calculation into Sentaurus' device solver using the Sentaurus Data Explorer[63], with a linear interpolation between the separately optimized optical and device meshes. We calculate electrical device performance considering Shockley-Read-Hall, Auger, and

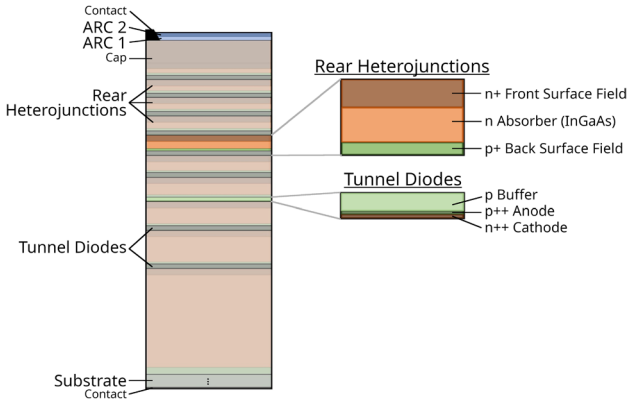

Fig. 1. Simplified schematic of the modeled devices, to scale with 98% total absorption Beer-Lambert absorber thicknesses (1550 nm illumination). Zoomed views (right) show the junction and tunnel diode construction. Colors indicate doping sign and concentration.

radiative recombination mechanisms. We include photon recycling and luminescent coupling, where photons originating in radiative recombination of carriers are reabsorbed in the device, with a custom python plugin using the iterative method of Wilkins et al. [64]. We calibrate the device model using experimental measurement of 1J, 2J, and 10J on-substrate PPCs[48,65] using PPCs grown and fabricated at Fraunhofer ISE[66] and experimentally characterized at Fraunhofer ISE[67] and the University of Ottawa SUNLAB[68,69]. Our rigorous calibration ensures accurate optimization results[48,70].

Figure 1 shows a schematic view of the 10J PPC devices in this paper including all modeled layers. We adopt the "segment" naming convention for same material subcells[53]; in this paper, using segment to refer to the subcell absorber layers specifically. We consider rear-heterojunction segments with high-bandgap front- and back-surface-field layers for efficient carrier extraction. The back-surface-field layer plays the role of emitter. The modeled tunnel diodes have negligible series resistance. We base their structure on Soresi et al. [71]. Allowing the ARC and the absorber layer thicknesses to vary under optimization results in the 12-dimensional (12D) design landscape of this study.

Optics-based photocurrent figure of merit

The typical figure of merit (FOM) in the design of PPCs is the optical to electrical power conversion efficiency, η_P, the ratio of electrical power out to photonic power in. In our model, the computational expense of the RCWA optical simulations is two to three orders of magnitude less than full optoelectronic device simulations. We introduce a FOM based on the optical part of the device simulation alone, this allows this study to be conducted with sufficient sample sizes in a reasonable time period. We calculate and report the full optoelectronic, η_P , for the top-performing designs only. Our optical-only photocurrent FOM, η_J,

$$\eta_J = \text{Photocurrent FOM} = \frac{\text{device photocurrent } [e/s]}{\text{incident photons per segment } [\gamma/s]}, \tag{1}$$

is the device photocurrent in number of electrons, *e*, per second calculated by the RCWA optical solver divided by one tenth of the input power in number of photons, γ, per second (the input power perfectly shared in the series-connected 10J device). The RCWA calculation accounts for reflection and transmission at all interfaces, as well as optical interference effects. The η_J accounts for current matching between the segments by taking the limiting segment photocurrent for the device. It has an ideal value of 1, which indicates the possibility of converting 100% of the incident light into equal numbers of carriers in each segment of the device.

The η_J proves to be a good proxy for full optoelectronic device efficiency under current matching conditions. Figure 2 shows the modeled η_P as a function of η_J for a large number of device designs over a wide η_J range. We simulate ten different randomly generated or partially optimized designs at each of 39 η_J values, given by the gray markers. The black markers indicate the average for each set of ten designs. The root-mean-square-error (RMSE) over each set is used for gray error bars. For this study, we consider the designs with the highest η_J . Figure 2 shows that these designs have the highest efficiencies and sit in a region of the plot where there is good correlation between the full optoelectronic η_P and the optical-only η_J. At lower η_J values, a greater variety in the optoelectronic performance of the designs emerges. This originates in the greater physical variety in the surveyed designs which can attain a given η_J when including luminescent coupling. Luminescent coupling naturally redistributes current when segments are current mismatched allowing a larger variety of designs to achieve high performance. In Fig. 2, this effect is especially evident in the device designs which achieve high η_P despite having non-optimal photocurrent FOM and is the reason why the correlation over the full η_J range is flatter than the highly current matched region ($\eta_J \geq 0.98$). Luminescent coupling is not included in the optical simulations.

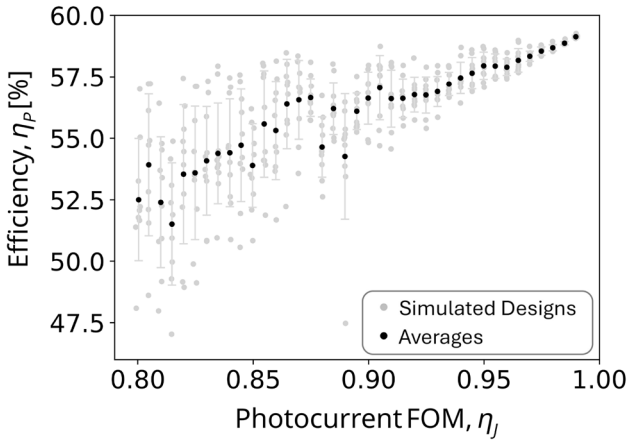

Fig. 2. Correlation between full optoelectronic device efficiency, η_P, and the optical-only FOM, η_J , for a large variety of designs. Ten different randomly generated or partially optimized designs are simulated at each sampled η_J value, given by the gray markers. Black markers indicate the average for each set of ten. RMSE error bars are given. Excellent correlation for the highest performing designs exists.

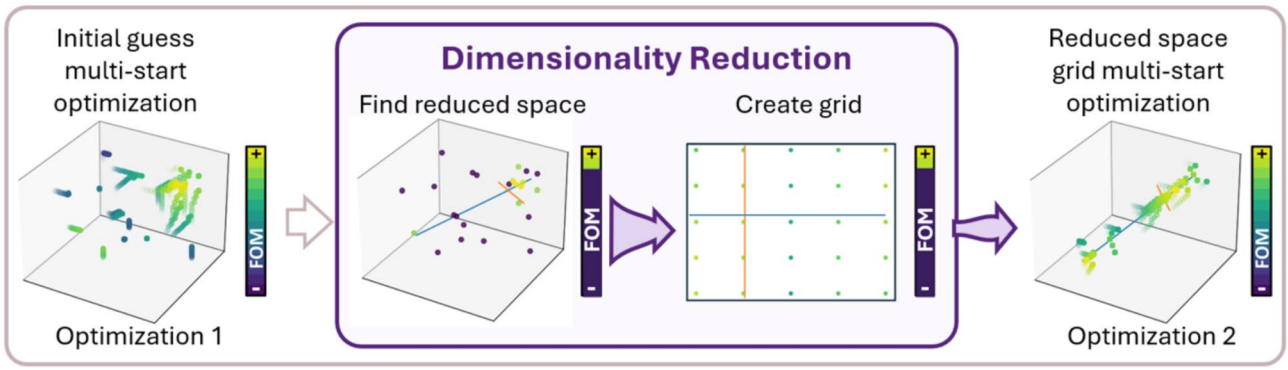

Fig. 3. Simplified design flow for the machine learning enhanced design optimization. Step 1; classical multi-start optimization. Step 2; top designs from step 1 according to a chosen figure of merit (FOM) are used to train a dimensionality reduction algorithm and generate a reduced dimension subspace. Step 3; the reduced dimensional subspace is used to generate start points. Step 4; extension of the method, classical multi-start optimization from the step 3 grid points to mitigate information loss during steps 2 and 3.

Machine learning enhanced optimization implementation

Our dimensionality reduction based design method is given in Fig. 3. It involves a four-step process. First, any classical multi-start optimization method produces a sparse set of high-performance designs (Optimization 1). Second, the top designs are used to train the dimensionality reduction algorithm, and a reduced dimensional subspace is constructed. Third, a grid of designs are generated in the reduced dimensional subspace. And fourth, these designs are used as starting points for a second stage of classical optimization in the full dimensional design space (Optimization 2). Previously, the first three steps of this method were used by Melati et al. to assist in the design of nanoscale silicon-on-insulator vertical grating couplers and power splitters[13–17,72]. We add the second optimization step to mitigate loss of information during the dimensionality reduction step (see the Results section and the first section of Supplementary 1 and Supplementary Fig. S1 for more information).

In this work, we generate the starting points for the first stage of optimization randomly in a hyperbox centered around the 98% total absorption Beer-Lambert absorber thicknesses and the ARC thicknesses from the calibration device[48]. We survey a wide area of the design landscape with the hyperbox edges at ±40% for the InGaAs layers and ±90% for the ARC layers. We generate 10,000 random designs. For optimization, we employ the Nelder-Mead simplex method, as we observe it to reach better performing designs compared to gradient based techniques. The optimizations are run until convergence for each design assuming default convergence tolerances[62]. We use the top 200 designs as training data for dimensionality reduction representing a η_J cutoff of 0.984.

The dimensionality reduction algorithm we use here is principal component analysis (PCA)[73,74]. As equation (2) shows, in PCA the reduced space dimensions, or "components", y_i, are created by linear combination of the input dimensions, x_j, which are standardized using a mean, μ_j, subtraction and standard deviation, σ_j, normalization. The algorithm operates to find the coefficients, a_{ij}, for the linear sums of the standardized input

dimensions, x'_j, with the a_{ij} chosen to retain the maximal amount of variance in the data. In other words, PCA operates to find the best linear dimensionality reduction solution with respect to the mean squared error measure of information loss leading to a_{ij} which are the coefficients for the ordered eigenvectors of the covariance matrix.

$$y_i = \sum_j a_{ij} \left(\frac{x_j - \mu_j}{\sigma_j} \right) = \sum_j a_{ij} x'_j, \tag{2}$$

We select the dimensionality of the reduced space based upon the ability to reconstruct the training data. We project the training data points into and back out of reduced spaces of different dimensionality and calculate the average error in their reconstruction. The blue trend in Fig. 4 shows the result of this analysis. The red trend in Fig. 4 shows a related measure: the percentage of training data variance each reduced space retains. In this study, we choose a reduced space dimensionality of three, as the smallest reduced space in the plateau of the reconstruction error trend. The average reconstruction error for this reduced space is 0.085 μm and the training data variance retained is ∼88%.

We generate a grid of approximately 10,000 new designs spread across the identified subspace, bounded by the extremities of the training data. We project these designs out into the original space where they are used as the starting points for the second stage of optimization. We then gather the final designs from both stages of optimization and apply constraints of 5 μm maximum for a single segment thickness and 8 μm maximum for the total absorber thickness. These constraints originate in practical limits on the total time and thermal budget allowances for growth of the epitaxial semiconductor structure.

The classical optimization only baseline uses the same simulation framework. To ensure a fair comparison, it uses two stages of optimization with the end points from the first stage used as the starting points for the second stage. This choice is equivalent to running the results from Optimization 1 directly into Optimization 2 without the dimensionality reduction steps in Fig. 3. The second optimization stage once again uses the Nelder-Mead algorithm with default convergence criteria. Both the ML-enhanced and classical-only methods use the same first stage data. We run our design optimization using common packages in a python environment called aiirmap[75]. We use scikit-learn[62] for machine learning and optimization algorithms. Databasing of the model results leverages pandas[76,77].

Results

Nature of ML-enhanced optimization and comparison to the conventional design

We show the nature of the optimized results from both optimization stages of the ML-enhanced method in Fig. 5. Supplementary Fig. S2 shows qualitatively similar results for the classical optimization. Figs. 5a and 5b plot the InGaAs segment absorber layer thicknesses against η_J. Figure 5a shows all absorber layer thicknesses, while Fig. 5b zooms in on the thinner layers . In Fig. 5c, we plot the optimized on-substrate designs as a function of the double-layer ARC thicknesses. Figure 5 shows over 19,000 designs. These are the designs which pass the growth constraints minus the few (197) optimized designs which have an η_J less than 0.80. We highlight the top designs, $\eta_J \geq 0.99$, on these plots using a vertical line and darker markers in Figs. 5a and 5b and orange markers in Fig. 5c. Nearly 4,000 designs meet this criteria. Using x's, we include a conventional Beer-Lambert design with 99.5% total absorption and η_J of 0.966. The highest performing designs achieve an η_J of 0.996.

Two features drive the η_J optimization: current matching between segments and maximizing absorber thickness. The former dominates with direct proportionality; any current mismatch directly lowers the total device current. Meanwhile, the latter inherits the logarithmic relation between thickness and absorption encoded in the physics of the Beer-Lambert relationship. Consequently, thin current matched devices with only ∼4.5 μm of absorber material can achieve reasonable η_J (∼0.95), while the highest η_J require current-matching and the exponentially thicker layers (most clearly observed in the segment 1 trend). The exponential-like absorption trend also reflects in the smaller thickness spread in the upper layers; they are more tightly constrained to obtain current matched values under the higher photon fluxes they experience. For the absolute highest η_J designs (∼

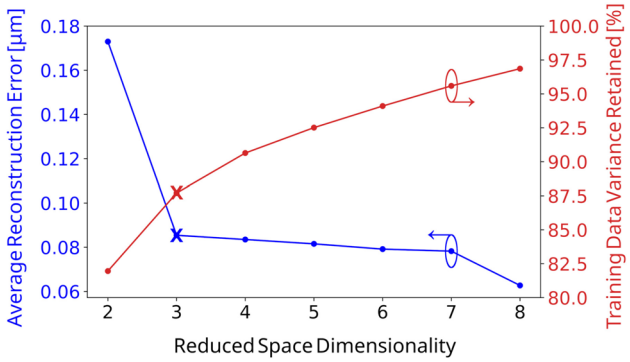

Fig. 4. Average reconstruction error of the 12-dimensional training data (blue, left axis) and percentage of training data variance retained (red, right axis) for reduced spaces of different dimensionality. The trends flatten out indicating a level of stability in the complexity of the data. The x's show the selected reduced space.

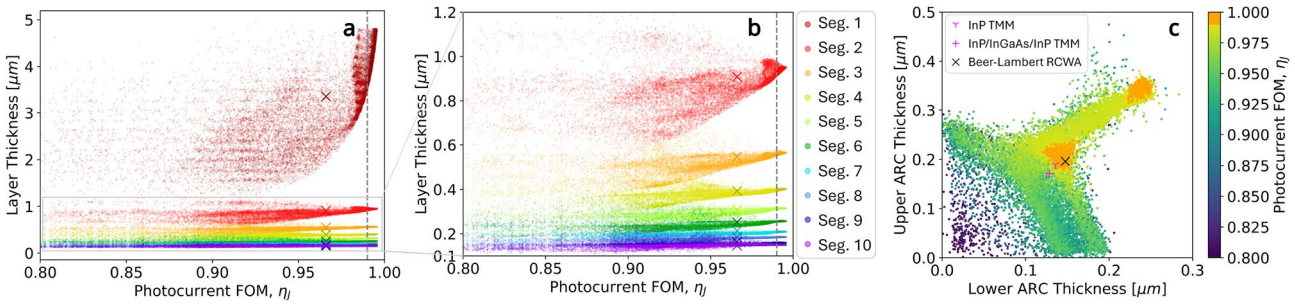

Fig. 5. Optimized layer thicknesses for the ML-enhanced method. **a** Segment absorber layer thicknesses as a function of η_J. **b** Zoom of **a** highlighting segments 2-10. The highest η_J designs show narrow distributions for all but segment 1 absorber thickness. **c** the η_J for all designs as a function of the double-layer anti-reflection coating thicknesses. Purple markers (Y and +) indicate ARC designs which use a simpler structure and optimization method (as detailed in the text). In all panels, the designs exceeding a η_J of 0.99 are indicated using darker markers. X's indicate the 99.5% total absorption Beer-Lambert absorber design.

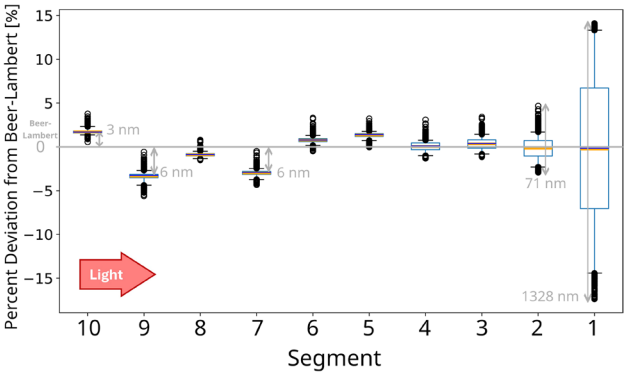

Fig. 6. Deviation of layer thicknesses of the top ($\eta_J \geq 0.99$) ML-enhanced designs from the 99.5% Beer-Lambert design. Orange lines denote mean values, blue lines denote medians, and the box gives the first and third quartiles. The whiskers show the two sigma extent of the data and open circles the designs falling outside these limits. Several segments (10, 9, and 7), have optimal layer thicknesses that are significantly (∼2-3%) different from the Beer-Lambert thicknesses.

0.996) a single solution for the absorber thicknesses exists. This solution differs systematically from the Beer-Lambert trend, as Fig. 6 will explore.

The segment 1 trend in Fig. 5a shows evidence of optical interference phenomena in the large number of horizontal ridges. These preferential thicknesses occur at half-wavelength optical path length intervals of the incident light indicating where the optimization stabilizes when the rate of change in the interference pattern and generation rate in the bottom segment are minimized. There is indication that segment 2 is also thick enough for this effect to occur. The maximum of 5 μm in Fig. 5a indicates the growth-informed design constraints.

The ML-enhanced optimization converges to two unique ARC designs, the two orange peaks in Fig. 5c. Figure 5c also shows several features associated with optical interference. Linear peaks of higher η_J extend outward from the x and y axes along lines which maximize transmission through the ARCs. The intersection at the y-axis is at the expected location, where the upper ARC has a quarter wavelength optical depth (refractive index of the upper ARC is 1.38 at 1.550 μm) and thus purely destructive interference upon reflection at the first interface. On the other hand, the intersection at the x-axis has been split to either side of the quarter wavelength optical depth in the lower ARC due to the presence of the InP window layer. The near half wavelength optical depth of the window leads to the small split and strong optical coupling which produces a second linear peak of high-performance. We find near-optimal performance along another linear trend which connects the two orange optimal performance peaks. This is associated with the current match layer pattern, with the two peaks indicating the designs where this layer pattern couples to an ∼5 μm thick segment 1. The second peak designates the interference modified half wavelength shift at which destructive interference between reflected waves is once again maximized.

The simple approach of optimizing the ARC layers separately from the absorber layers proves to be sufficient in this device architecture. The purple markers in Fig. 5c indicate double-layer ARC thicknesses optimized using the transfer matrix method on-top of simpler epitaxial layer stacks. For the purple tri marker (Y), the underlying structure is an InP substrate only, for the purple plus marker (+) the ARCs sit atop 1 μm InP, 2 μm InGaAs, and an InP substrate. The black x indicates the fully modeled layer stack with Beer-Lambert absorber thicknesses

(as in Fig. 1). These three ARC designs are similar, with single-layer ARC thicknesses differing by 25 nm or less. Under optoelectronic simulation using the Beer-Lambert absorber design, we obtain negligible performance loss for devices where the ARCs were optimized using the simpler structure.

The ML-enhanced optimized absorber thicknesses systematically deviate away from the simple Beer-Lambert exponential absorption trend. Figure 6 shows the percent difference between the top ($\eta_J \geq 0.99$) ML-enhanced optimized segment thicknesses compared to the 99.5% absorption Beer-Lambert design shown by the x's in Fig. 5. This Beer-Lambert design is chosen such that the bottom segment thickness aligns with the mean optimized value. It corresponds to a Beer-Lambert device with total absorber thickness of 7.4 μm. In Fig. 6, segments 10, 6, and 5 are, on average, slightly thicker than the Beer-Lambert while the remaining upper segments are up to ∼3% thinner. The maximal average percent difference is 3.3%, this was obtained for segment 9 and corresponds to a 6 nm thickness difference. Spreads in the optimized thickness remain ∼5% for all but the thickest segments, where they increase to 8% and ∼31% (+14% to -17%) in segments 2 and 1 respectively. Similar results are found for the classically optimized dataset (see Supplementary Fig. S3). We attribute these deviations to optical interference effects in the multilayer cavity which are strongest at the thinner top segments (see Supplementary Fig. S4 for more information). This optical interference arises from differences in refractive index between layers which produce multiple reflections and a weak Fabry-Perot type resonance effect. Features which are not captured in the Beer-Lambert approach. The design differences do not prove meaningful under full optoelectronic simulation with luminescent coupling. The natural current redistributing recovery of the luminescent coupling process (see Fig. 2) leads to equivalent optoelectronic power conversion efficiencies for the Beer-Lambert design and the top ML-optimized devices from each ARC cluster. Furthermore, the deviations observed in the mean optimized layer thicknesses in Fig. 6 fall within the typical uncertainty arising in the epitaxial growth which leads to layer thicknesses that vary by up to 5% of their nominal value. While these results remain of theoretical interest only for the 10J on-substrate InGaAs devices studied here, optimal layer thickness modulation due to optical interference effects may play a larger role in PPC devices with different materials, junction multiplicities, refractive index variations, auxiliary layer designs, or device architectures (such as thin film PPCs with a back-reflector instead of the substrate[78]). In this design and with efficiency as the target figure of merit, these results give confidence to designers employing the Beer-Lambert approach for the absorber layer thicknesses.

Comparison between ML-enhanced and classical design optimizations

By comparing the η_J and variety of the optimized designs we find that the ML-enhanced method outperforms the classical optimization method in a number of ways. Figure 7 shows the η_J population probability distributions for the designs after the first stage of optimization (yellow, Fig. 3 Optimization 1), from the reduced dimensional space grid (light blue), after the second stage of optimization starting from the reduced space grid (dark blue, ML-enhanced, Fig. 3 Optimization 2), and after the second stage of optimization starting from the first stage end-points (brown, classical). We do not include the initial random starting point designs, they had a normally distributed η_J histogram with a mean of ∼0.58 and a standard deviation of ∼0.08. The differences in the populations arise from the application of the growth constraints, the reduced space grid granularity, and from simulations which fail to converge.

The reduced dimensional subspace is highly effective at generating second stage optimization starting points and accelerates design discovery further down the optimization pathway. As Fig. 7 shows, over forty percent of the points from the ML-enhanced second stage reach the highest η_J (≥ 0.99). This compares to only ∼4% for the classical optimization second stage. The very top performing designs from both methods have nearly equivalent performance (η_J of 0.995 (classical) and 0.996 (ML-enhanced)) but there are over 20 times as many designs at this level for the ML-enhanced method compared to the classical method. The lowest performing design after the ML-enhanced second stage has an η_J of 0.971; ∼60% of the designs from the classical second stage do not reach this mark. The ML method also produces more significantly thicker devices (e.g. 43% of designs thicker than 7 μm, comparing to 9% for classical second stage) indicating it has proceeded further along

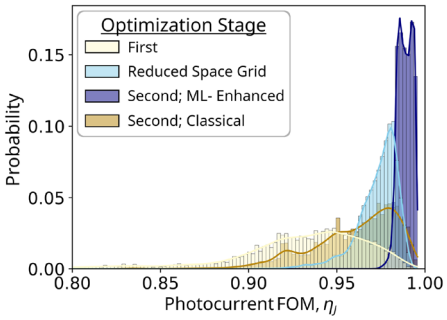

Optimization Stage	Total Population	Average η_J	Population $\eta_J \geq 0.99$
First	9922	0.928	24 (0.2%)
Reduced Space Grid	10316	0.973	70 (0.7%)
Second; ML-Enhanced	9423	0.989	3890 (41.3%)
Second; Classical	9718	0.959	417 (4.3%)

Fig. 7. Photocurrent FOM population probability histograms for designs from different stages of the ML-enhanced and classical optimization scenarios. The total design populations meeting the growth constraints, the number and percentage of these designs with a η_J greater than or equal to 0.99, and average η_J for each stage are also given. This shows the much larger number and percentage of high-η_J designs produced by the ML-enhanced method.

the optimization pathway. In Fig. 7, the double peak in the ML-enhanced second stage data reflects results which straddle the saddle region within the ARC subspace (the yellow area between the two orange peaks in Fig. 5c). The peaks are centered at η_J of 0.986 and 0.994.

We obtain the optimized designs from the ML-enhanced second stage of optimization with 30% less computational effort compared to the classical second stage of optimization, as measured by the average number of iterations until convergence. The total reduction in computational cost is 15% for the full method (steps 1 through 4 of Fig. 3) compared to the classical optimization method since both approaches use the same first stage data which had a similar computational cost as the classical second stage. The dimensionality reduction step itself is computationally inexpensive.

The reduced dimensional subspace grid survey, light blue in Fig. 7, produces a large quantity of near-optimal designs (≥ 0.95). The reduced space is constructed from first stage training data with an η_J cutoff of 0.984. We attribute the η_J tail below the training data threshold to a small loss of meaningful information which occurs during the grid creation and results in a reduced space which includes the high performance peak as well as a slightly lower performance volume (in this case, the saddle region within the ARC subspace). This loss of information motivates our second stage of optimization (see the first section of Supplementary 1).

The ML-enhanced optimization also demonstrates greater variability of top performing designs when we compare to those generated using the classical two-stage optimization. Fig. 8 shows the designs with η_J greater than or equal to 0.99 after the ML-enhanced and classical second stage for two 2D projections of the 12D design space. Shared xy axes highlight the extended variety of the designs that the ML-enhanced procedure attains. In the ARCs (top row of Fig. 8 and Fig. 5c) we find that the ML-enhanced method generates a much greater population of designs with thicker ARC layers. While this thicker ARC design is expected from simple optics and is not typically considered in fabrication of real devices, this result shows the potential of the dimensionality reduction enhanced method to move out, discover, and populate new high performance regions of the design space. The thicker ARC peak being in an area outside the range of the initial guesses and only sparsely present in the training data. The segment 2 - segment 3 projections (bottom row of Fig. 8) show a variation which is mirrored across the absorber design space and arises as all layers shift according to the interference patterns to maintain segment current matching. This variety may allow discovery of designs which satisfy multiple performance metrics and/or are less sensitive to typical design parameter variations in realistic devices and their operation (e.g. temperature, wavelength, absorber composition, thickness accuracy and precision).

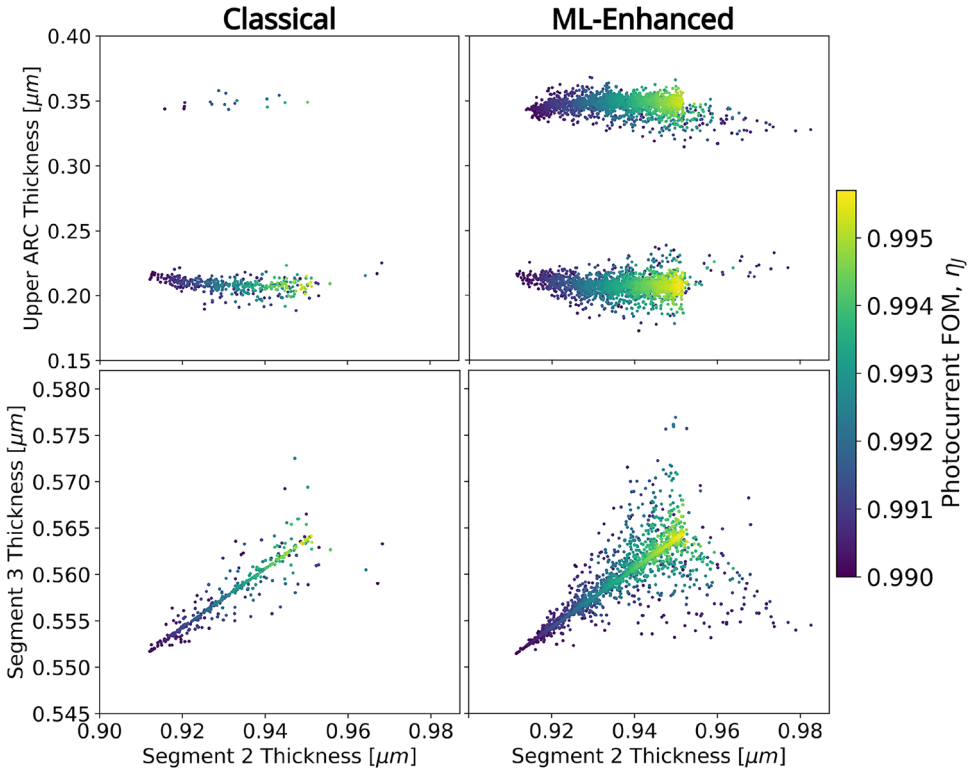

Fig. 8. Two-dimensional projections, selected from the 12-dimensional design space. The high-η_J (≥ 0.99) designs from the classical optimization (left) and ML-enhanced (right) second stages of optimization. The thicknesses of the upper ARC (top) and segment 3 (bottom) are shown against the segment 2 thickness. The larger number of designs, higher η_J , and larger diversity of designs from the ML-enhanced method is clear.

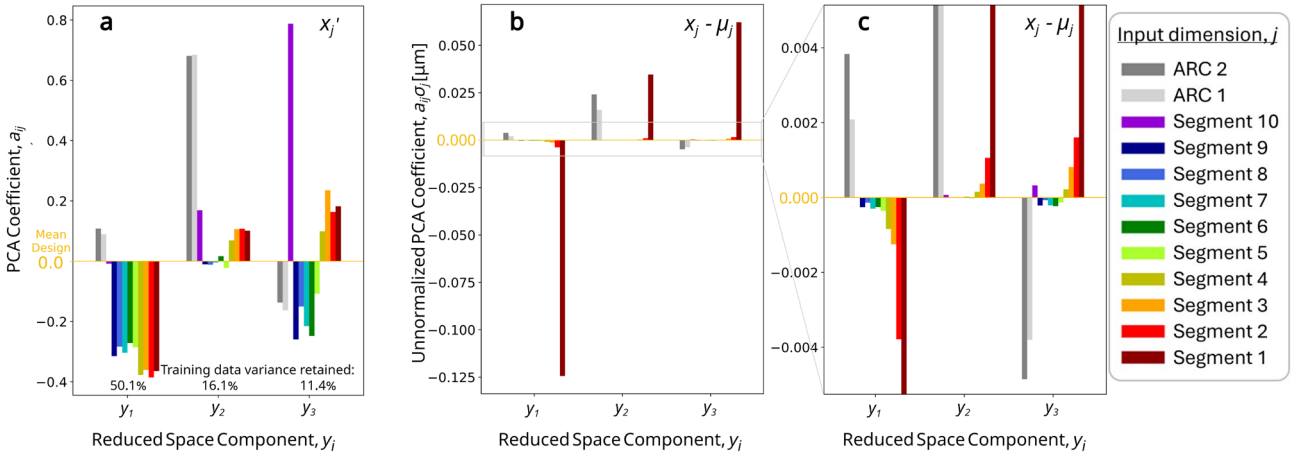

Fig. 9. Reduced dimensionality subspace construction for the first three principal components that principal component analysis identifies. **a** PCA coefficient, a_{ij} of equation (2), for each standardized input dimension, x_j'. **b** PCA coefficient times the standard deviation, $a_{ij} * \sigma_j$, in micron, for each mean subtracted input dimension, $x_j - \mu_j$. **c** Y-scale zoom on the zero region of **b**. The percent of training data variance which each of principal component retains is given along the bottom of **a**. The primary optical phenomena in the design space are visibly encoded in the construction of the reduced space.

Knowledge discovery through reduced dimensional subspace construction

Dimensionality reduction compresses this multi-junction PPC design space to one-quarter of its original size while maintaining an average reconstruction error of less than 100 nm. A number which is weighted by the thick bottom segments. The total training data variance that the three-dimensional space retains is 88%. Figure 9 presents the composition of the three principal components, the y_i in equation (2). Fig. 9a gives the reduced space construction in terms of the PCA coefficients, a_{ij}, for each standardized input dimension, x_j'. Fig. 9b and 9c remove the standard deviation normalization from the input dimensions to show the physical nature of the component composition. Due to the mean subtraction in equation (2), the zero of these plots represents the mean design, given by the orange lines in Fig. 6.

PCA determines the sets of correlations which account for the most variance in the training data. Components are constructed as orthonormal representations of these correlations. Within one component, same (opposite) sign coefficients indicate positive (negative) correlation between input dimensions, and the magnitude of each coefficient indicates how strongly each input dimension contributes to the trend. The sign and magnitude differences of the input dimension coefficients from one component to another have little physical meaning. The component ordering gives the relevant ordering of which trend contributes more to overall data variance[73]. We consider this when interpreting the reduced space construction for knowledge discovery.

The first principal component, y_1 in Fig. 9, encodes the most basic relationship in terms of the thickness dependencies between segments. It says that if one layer thickness increases, the others tend to increase to maintain current matching. As Fig. 9b shows, it implicitly encodes the Beer-Lambert like exponential relation between segment thicknesses. The first principal component accounts for ~69% of the training data variance.

The two ARC layers dominate the construction of the second principal component, y_2. Fig. 9a shows that over 13% of the variance in the training data was contained in these two dimensions alone. This signifies PCA's recognition of the two ARC peaks in the training data and the construction of a component which linearly spans the space between them.

The third principal component, y_3, forms the secondary axis of the ARC saddle (Fig. 5c). It also seems to encode a wave-like pattern through the absorber layers. This suggests the appearance of the optical interference phenomena we observed in the previous figures. Here, combined with the Beer-Lambert trend in y_1. Further testing suggests that 5-15% of the training data variance is attributable to optical interference phenomena (see Supplementary Fig. S5).

Discussion and conclusion

We study a ML-enhanced method which accelerates the design optimization of multi-junction PPCs. It produces a much greater number of designs attaining the highest η_J, these have a greater design variability, and are obtained at a lower computational cost than those found using classical optimization algorithms alone. These advantages, coupled with the demonstrated knowledge discovery, exemplify an expansion in the design perspective which empowers the design choice under external constraints and preferences (e.g. different or multiple performance metrics, growth parameters, or cost). In this study, the reduced space grid is conservatively bounded by the training data. Extending the grid beyond these bounds, or increasing the resolution of the grid survey, could lead to the generation of greater numbers of high-performance designs with larger variability.

We show the potential for knowledge discovery implicit in the construction of the reduced dimensional subspace. Figure 9 confirms the basic understanding of the multi-junction PPC design space. The major contributions to η_J are (y_1) the requirement for good current matching with Beer-Lambert like absorption, (y_2)

the optimization of the ARC, and (y_3) a fine-tuning of absorber thicknesses suggestive of optical interference effects within the multi-layer semiconductor stack. We attribute the deviations away from the Beer-Lambert design, as observed in Fig. 6, to this optical interference. Further knowledge discovery is possible within the on-substrate PPC context by including more design parameters, such as layer doping and auxiliary layer design, in the analysis.

The ML-enhanced method does not identify designs with higher optoelectronic efficiency than the conventional and classical approaches. This result is not unusual since the ML method relies on the same classical optimization algorithms to generate its designs. However, the larger variety in the ML-enhanced designs indicate that our method has led to a wider characterization of the high performance design space and lends stronger support to the conclusion that the Beer-Lambert approach is sufficient for the multi-junction PPC design problem when power conversion efficiency is the target figure of merit. In general, it is difficult to know apriori whether the ML-enhanced method will lead to new knowledge beyond what is known through classical or individually optimized means. In any case, dimensionality reduction offers an efficient pathway for a more complete characterization of the design space ensuring that nothing has been missed while simultaneously offering new design perspectives through knowledge discovery and a reduction in computational cost.

Optical-based design optimization of multi-junction PPCs ignores the important optoelectronic phenomenon known as luminescent coupling. As Fig. 2 shows, luminescent coupling can expand the pertinent design space if the highest efficiency is not the only performance criterion. Having multiple FOMs is often the case in reality, as applications, cost, manufacturing uncertainties, and operational uncertainties impose challenges and considerations beyond what can be easily simulated. Forcade et al. [48] show that PPCs optimized with luminescent coupling converge toward a layer structure with current limiting top and bottom junctions which take advantage of the physics of radiative recombination recapture. Future dimensionality reduction studies could use devices optimized with luminescent coupling, leading to an even larger diversity of high efficiency structures.

Machine learning is a toolbox of empowering methods which expands the design perspective in photovoltaics, optoelectronics, and beyond. By allowing a significant reduction in the complexity of a problem in a meaningful manner, dimensionality reduction simultaneously reduces computational cost while unlocking new pathways for exploration and fundamental understanding. It is an indispensable tool in the emerging field of ML-enhanced design, especially for high-dimensional problems. The general dimensionality reduction method we present here is applicable to problems that can be accurately numerically modeled. It does not require assumptions about the nature of the design space or on the optimization figure of merit but it requires an accurate model and a reasonably efficient optimization pipeline. This pipeline must generate a sufficient number of optimized and unbiased designs required for effective training. The general dimensionality reduction method can also be augmented by including other dimensionality reduction algorithms in place of principal component analysis, such as non-linear techniques[18,20–22,79] or feature selection[79,80]. It can be combined with other machine learning techniques such as neural networks and advanced optimization algorithms[2,3,6–9].

Data availibility

Data underlying the results presented in this paper are not publicly available at this time but may be obtained from the authors upon reasonable request. Please contact rhunt013@uottawa.ca.

Received: 28 March 2025; Accepted: 14 August 2025
Published online: 26 September 2025

References

1. Chen, H., Jia, H., Wang, T. & Yang, J. A gradient-oriented binary search method for photonic device design. *J. Light. Technol.* **39**, 2407–2412. https://doi.org/10.1109/JLT.2021.3050771 (2021).
2. Mao, S. et al. Inverse design for silicon photonics: From iterative optimization algorithms to deep neural networks. *Appl. Sci.* **11**, 3822. https://doi.org/10.3390/app11093822 (2021).
3. Yao, K., Unni, R. & Zheng, Y. Intelligent nanophotonics: merging photonics and artificial intelligence at the nanoscale. *Nanophotonics* **8**, 339–366. https://doi.org/10.1515/nanoph-2018-0183 (2019).
4. Ngatchou, P., Zarei, A. & El-Sharkawi, A. *Pareto multi objective optimization.* **2005**, 84–91. https://doi.org/10.1109/ISAP.2005.1599245 (2005).
5. Ma, W. et al. Deep learning for the design of photonic structures. *Nat. Photonics* **15**, 77–90 (2021).
6. Ren, Y. et al. Genetic-algorithm-based deep neural networks for highly efficient photonic device design. *Photonics Res.* **9**, B247. https://doi.org/10.1364/PRJ.416294 (2021).
7. Deng, L., Xu, Y. & Liu, Y. Hybrid inverse design of photonic structures by combining optimization methods with neural networks. *Photonics Nanostructures - Fundam. Appl.* **52**, 101073. https://doi.org/10.1016/j.photonics.2022.101073 (2022).
8. Jiang, J., Chen, M. & Fan, J. A. Deep neural networks for the evaluation and design of photonic devices. *Nat. Rev. Mater.* **6**, 679–700. https://doi.org/10.1038/s41578-020-00260-1 (2020).
9. Hegde, R. S. Deep learning: a new tool for photonic nanostructure design. *Nanoscale Adv.* **2**, 1007–1023. https://doi.org/10.1039/C9NA00656G (2020).
10. Adibnia, E., Ghadrdan, M. & Ali Mansouri-Birjandi, M. Chirped apodized fiber bragg gratings inverse design via deep learning. *Opt. Laser Technol* **181**, 111766. https://doi.org/10.1016/j.optlastec.2024.111766 (2025).
11. Adibnia, E., Ghadrdan, M. & Mansouri-Birjandi, M. A. Inverse design of fbg-based optical filters using deep learning: A hybrid cnn-mlp approach. *J. Light. Technol.* **43**, 4452–4461. https://doi.org/10.1109/JLT.2025.3534275 (2025).
12. Kiarashinejad, Y., Abdollahramezani, S. & Adibi, A. Deep learning approach based on dimensionality reduction for designing electromagnetic nanostructures. *npj Comput. Mater.* **6**(1), 12. https://doi.org/10.1038/s41524-020-0276-y (2020).
13. Melati, D. et al. Mapping the global design space of nanophotonic components using machine learning pattern recognition. *Nat. Commun.* **10**, 4775. https://doi.org/10.1038/s41467-019-12698-1 (2019).
14. Kamandar Dezfouli, M. et al. Perfectly vertical surface grating couplers using subwavelength engineering for increased feature sizes. *Opt. Lett.* **45**, 3701. https://doi.org/10.1364/OL.395292 (2020).

15. Melati, D. et al. Design of multi-parameter photonic devices using machine learning pattern recognition. In Baets, R. G., O'Brien, P. & Vivien, L. (eds.) *Integrated Photonics Platforms: Fundamental Research, Manufacturing and Applications*, 7, https://doi.org/10.1117/12.2559583 (SPIE, 2020).
16. Melati, D. et al. Design of compact and efficient silicon photonic micro antennas with perfectly vertical emission. *IEEE J Sel. Top. Quantum Electron.* **27**, 1–10. https://doi.org/10.1109/JSTQE.2020.3013532 (2021).
17. Melati, D. et al. Subwavelength metamaterial devices with optimization and machine learning. In He, S. & Vivien, L. (eds.) *Smart Photonic and Optoelectronic Integrated Circuits 2023*, vol. PC12425, PC1242509, https://doi.org/10.1117/12.2649953. International Society for Optics and Photonics (SPIE, 2023).
18. Al-Digeil, M. et al. Pca-enhanced autoencoders for nonlinear dimensionality reduction in low data regimes. In *Proceedings of the 36th Canadian Conference on Artificial Intelligence*, https://doi.org/10.21428/594757db.05a13011 (Canadian Artificial Intelligence Association, 2023).
19. Zandehshahvar, M., Hemmatyar, O., Kiarashinejad, Y., Abdollahramezani, S. & Adibi, A. Dimensionality reduction based method for design and optimization of optical nanostructures using neural network. In *Frontiers in Optics + Laser Science APS/DLS*, FM5C.2, https://doi.org/10.1364/FIO.2019.FM5C.2 (OSA, 2019).
20. Kudyshev, Z. A., Kildishev, A. V., Shalaev, V. M. & Boltasseva, A. Machine learning–assisted global optimization of photonic devices. *Nanophotonics* **10**, 371–383. https://doi.org/10.1515/nanoph-2020-0376 (2020).
21. Liu, Z., Raju, L., Zhu, D. & Cai, W. A hybrid strategy for the discovery and design of photonic structures. *IEEE J. Emerg. Sel. Top. Circuits Syst.* **10**, 126–135. https://doi.org/10.1109/JETCAS.2020.2970080 (2020).
22. Liu, Z. et al. Compounding meta-atoms into metamolecules with hybrid artificial intelligence techniques. *Adv. Mater.* **32**, 1904790. https://doi.org/10.1002/adma.201904790 (2020).
23. Kiarashinejad, Y., Abdollahramezani, S., Zandehshahvar, M., Hemmatyar, O. & Adibi, A. Deep learning reveals underlying physics of light–matter interactions in nanophotonic devices. *Adv. Theory Simul.* **2**, 1900088. https://doi.org/10.1002/adts.201900088 (2019).
24. Kiarashinejad, Y. et al. Knowledge discovery in nanophotonics using geometric deep learning. *Adv. Intell. Syst.* **2**, 1900132. https://doi.org/10.1002/aisy.201900132 (2020).
25. Hemmatyar, O., Abdollahramezani, S., Kiarashinejad, Y., Zandehshahvar, M. & Adibi, A. Full color generation with Fano-type resonant HfO $_2$ nanopillars designed by a deep-learning approach. *Nanoscale* **11**, 21266–21274. https://doi.org/10.1039/C9NR07408B (2019).
26. Matsuura, M. Recent advancement in power-over-fiber technologies. *Photonics* **8**, 335. https://doi.org/10.3390/photonics8080335 (2021).
27. Fafard, S. & Masson, D. P. Perspective on photovoltaic optical power converters. *J. Appl. Phys.* **130**, 160901. https://doi.org/10.1063/5.0070860 (2021).
28. Algora, C. et al. Beaming power: Photovoltaic laser power converters for power-by-light. *Joule* **6**, 340–368. https://doi.org/10.1016/j.joule.2021.11.014 (2022).
29. Putra, E. P. et al. Technology update on patent and development trend of power over fiber: a critical review and future prospects. *J. Photonics Energy* **13**(1), 011001–011001. https://doi.org/10.1117/1.JPE.13.011001 (2023).
30. Spillman, W., Crowne, D. & Woodward, D. Optically powered and interrogated rotary position sensor for aircraft engine control applications. *Opt. Lasers Eng.* **16**, 105–118. https://doi.org/10.1016/0143-8166(92)90003-P (1992).
31. Worms, K. et al. Reliable and lightning-safe monitoring of wind turbine rotor blades using optically powered sensors. *Wind Energy* **20**, 345–360. https://doi.org/10.1002/we.2009 (2017).
32. De Nazare, F. V. B. & Werneck, M. M. Hybrid optoelectronic sensor for current and temperature monitoring in overhead transmission lines. *IEEE Sens. J.* **12**, 1193–1194. https://doi.org/10.1109/JSEN.2011.2163709 (2012).
33. Zheng, Y. et al. Wireless laser power transmission: Recent progress and future challenges. *Space Sol. Power Wirel. Transm.* S2950104023000020, https://doi.org/10.1016/j.sspwt.2023.12.001 (2024).
34. Ding, J., Liu, W., I, C.-L., Zhang, H. & Mei, H. Advanced progress of optical wireless technologies for power industry: An overview. *Appl. Sci.* **10**(8), 6463. https://doi.org/10.3390/app10186463 (2020).
35. Zin, A. M., Bongsu, M. S., Idrus, S. M. & Zulkifli, N. An overview of radio-over-fiber network technology. *In Int. Conf. Photonics* **1–3**, 2010. https://doi.org/10.1109/ICP.2010.5604429 (2010) ((**IEEE**)).
36. Aboelala, O., Lee, I. E. & Chung, G. C. A survey of hybrid free space optics (FSO) communication networks to achieve 5g connectivity for backhauling. *Entropy* **24**, 1573. https://doi.org/10.3390/e24111573 (2022).
37. Goto, K., Nakagawa, T., Nakamura, O. & Kawata, S. An implantable power supply with an optically rechargeable lithium battery. *IEEE Trans. Biomed. Eng.* **48**, 830–833. https://doi.org/10.1109/10.930908 (2001).
38. Vazquez, C. et al. Multicore fiber scenarios supporting power over fiber in radio over fiber systems. *IEEE Access* **7**, 158409–158418. https://doi.org/10.1109/ACCESS.2019.2950599 (2019).
39. Al-Zubaidi, F. M. A., Lopez-Cardona, J. D., Sanchez Montero, D. & Vazquez, C. Optically powered radio-over-fiber systems in support of 5g cellular networks and IoT. *J. Light. Technol.* **39**, 4262–4269. https://doi.org/10.1109/JLT.2021.3074193 (2021).
40. Grandidier, J. et al. Feasibility of power beaming through the venus atmosphere. *Acta Astronautica* **211**, 376–381. https://doi.org/10.1016/j.actaastro.2023.06.042 (2023).
41. Malaviya, P., Sarvaiya, V., Shah, A., Thakkar, D. & Shah, M. A comprehensive review on space solar power satellite: an idiosyncratic approach. *Environ. Sci. Pollut. Res.* **29**, 42476–42492. https://doi.org/10.1007/s11356-022-19560-w (2022).
42. Guiomar, F. P., Fernandes, M. A., Nascimento, J. L., Rodrigues, V. & Monteiro, P. P. Coherent free-space optical communications: Opportunities and challenges. *J. Light. Technol.* **40**, 3173–3186. https://doi.org/10.1109/JLT.2022.3164736 (2022).
43. Jahid, A., Alsharif, M. H. & Hall, T. J. A contemporary survey on free space optical communication: Potentials, technical challenges, recent advances and research direction. *J. Netw. Comput. Appl.* **200**, 103311. https://doi.org/10.1016/j.jnca.2021.103311 (2022).
44. Dahrouj, H., Douik, A., Rayal, F., Al-Naffouri, T. Y. & Alouini, M.-S. Cost-effective hybrid RF/FSO backhaul solution for next generation wireless systems. *IEEE Wirel. Commun.* **22**, 98–104. https://doi.org/10.1109/MWC.2015.7306543 (2015).
45. Fafard, S. & Masson, D. P. High-efficiency and high-power multijunction InGaAs/InP photovoltaic laser power converters for 1470 nm. *Photonics* **9**, 438. https://doi.org/10.3390/photonics9070438 (2022).
46. Lozano, J. F. et al. A new path towards ultra-high efficient laser power converters: Silicon carbide-based multijunction devices. *Results Eng.* **21**, 101987. https://doi.org/10.1016/j.rineng.2024.101987 (2024).
47. Helmers, H. et al. Photovoltaic cells with increased voltage output for optical power supply of sensor electronics. In *Proceedings SENSOR 2015*, 519–524. https://doi.org/10.5162/sensor2015/D1.4 (2015) ((**AMA Service GmbH, Von-Münchhausen-Str. 49, 31515 Wunstorf, Germany**)).
48. Forcade, G. P. et al. 53.6% efficient multi-junction laser power converter for extended telecom range operation. Manuscript submitted for publication (2024).
49. Zhao, Y., Sun, Y., He, Y., Yu, S. & Dong, J. Design and fabrication of six-volt vertically-stacked GaAs photovoltaic power converter. *Sci. Rep.* **6**, 38044. https://doi.org/10.1038/srep38044 (2016).
50. Fafard, S. et al. Power and spectral range characteristics for optical power converters. *Energies* **14**, 4395. https://doi.org/10.3390/en14154395 (2021).
51. Fafard, S. et al. High-efficiency photovoltaic power converters and application to optical power transmission. In *2021 26th Microoptics Conference (MOC)*, 1–2, https://doi.org/10.23919/MOC52031.2021.9598073 (IEEE, 2021).

52. Hunter, R. F. H., Valdivia, C. E., Baribeau, L. S. & Hinzer, K. Unlocking the potential for extreme solar concentration via subcell segmentation. In *17th International Conference on Concentrator Photovoltaic Systems (CPV))*, 020006, https://doi.org/10.1063/5.0099470 (2022).
53. Valdivia, C. E. & Hinzer, K. Subcell segmentation for current matching and design flexibility in multijunction solar cells. *IEEE J. Photovolt.* **10**, 1329–1339. https://doi.org/10.1109/JPHOTOV.2020.3005630 (2020).
54. Baribeau, L. S., Hunter, R. F., Valdivia, C. E. & Hinzer, K. Drift-diffusion modelling of four-junction ingap/ingaas/sigesn/ge solar cells. In *2022 IEEE 49th Photovoltaics Specialists Conference (PVSC)*, 1031–1031, https://doi.org/10.1109/PVSC48317.2022.9938603 (2022).
55. Fafard, S. et al. Ultrahigh efficiencies in vertical epitaxial heterostructure architectures. *Appl. Phys. Lett.* **108**, 071101. https://doi.org/10.1063/1.4941240 (2016).
56. Fafard, S. & Masson, D. Vertical multi-junction laser power converters with 61% efficiency at 30 w output power and with tolerance to beam non-uniformity, partial illumination, and beam displacement. *Photonics* **10**, https://doi.org/10.3390/photonics10080940 (2023).
57. Mukherjee, J., Jarvis, S., Perren, M. & Sweeney, S. J. Efficiency limits of laser power converters for optical power transfer applications. *J. Phys. D Appl. Phys.* **46**, 264006. https://doi.org/10.1088/0022-3727/46/26/264006 (2013).
58. Beattie, M. N. et al. InP- and GaAs-based photonic power converters under o-band laser illumination: Performance analysis and comparison. *IEEE J. Photovolt.* **13**, 113–121. https://doi.org/10.1109/JPHOTOV.2022.3218938 (2023).
59. Synopsys Inc. Sentaurus TCAD user guide version S-2021.06 (2021).
60. Liu, V. & Fan, S. S^4: A free electromagnetic solver for layered periodic structures. *Comput. Phys. Commun.* **183**, 2233–2244. https://doi.org/10.1016/j.cpc.2012.04.026 (2012).
61. Pearce, P. & Liu, V. S4 - RCWA. github https://github.com/phoebe-p/S4 (retrieved Jan. 2023).
62. Pedregosa, F. et al. Scikit-learn: Machine learning in python. *J. Mach. Learn. Res.* **12**, 2825–2830. https://doi.org/10.5555/1953048.2078195 (2011).
63. Synopsys Inc. Sentaurus data explorer user guide version S-2021.06 (2021).
64. Wilkins, M. et al. Luminescent coupling in planar opto-electronic devices. *J. Appl. Phys.* **118**, 143102. https://doi.org/10.1063/1.4932660 (2015).
65. Forcade, G. P. et al. High-performance multi-junction c-band photonic power converters: Calibrated optoelectronic model for next generation designs. In *2023 IEEE 50th Photovoltaic Specialists Conference (PVSC)*, https://doi.org/10.1109/PVSC48320.2023.10359786 (2023).
66. Helmers, H. et al. Advancing solar energy conversion efficiency to 47.6% and exploring the spectral versatility of III-V photonic power converters. In Freundlich, A., Collin, S., Hinzer, K. & Sellers, I. R. (eds.) Physics, Simulation, and Photonic Engineering of Photovoltaic Devices XIII, vol. 12881, 1288103, https://doi.org/10.1117/12.3000352. International Society for Optics and Photonics (SPIE, 2024).
67. Helmers, H. et al. Unlocking 1550 nm laser power conversion by ingaas single- and multi-junction pv cells. In *2022 IEEE 49th Photovoltaics Specialists Conference (PVSC)*, 9938627, 1235–1235, https://doi.org/10.1109/PVSC48317.2022.9938627 (2022).
68. Beattie, M. N. et al. EQE measurement technique for multi-junction photovoltaics with overlapping subcell absorptance. In Freundlich, A., Collin, S., Hinzer, K. & Sellers, I. R. (eds.) Physics, Simulation, and Photonic Engineering of Photovoltaic Devices XIII, vol. PC12881, PC1288107, https://doi.org/10.1117/12.3001662. International Society for Optics and Photonics (SPIE, 2024).
69. Wilson, P. et al. Quantifying the luminescent coupling process in C-band multi-junction photonic power converters. In Freundlich, A., Collin, S., Hinzer, K. & Sellers, I. R. (eds.) Physics, Simulation, and Photonic Engineering of Photovoltaic Devices XIII, vol. PC12881, PC128810J, https://doi.org/10.1117/12.3000797. International Society for Optics and Photonics (SPIE, 2024).
70. Piprek, J. Simulation-based machine learning for optoelectronic device design: perspectives, problems, and prospects. *Opt. Quantum Electron.* **53**(4), 175. https://doi.org/10.1007/s11082-021-02837-8 (2021).
71. Soresi, S. et al. Inp:s/alinas:c tunnel junction grown by movpe for photovoltaic applications. *Phys. Status Solidi (A)* **215**, 1700427. https://doi.org/10.1002/pssa.201700427 (2018).
72. Melati, D. et al. Machine learning design of subwavelengh integrated photonic devices. In *2019 International Conference on Numerical Simulation of Optoelectronic Devices (NUSOD)*, 135–136, https://doi.org/10.1109/NUSOD.2019.8806835 (IEEE, 2019).
73. Jolliffe, I. T. & Cadima, J. Principal component analysis: a review and recent developments. *Philos. Transactions Royal Soc. A: Math. Phys. Eng. Sci.* **374**, 20150202. https://doi.org/10.1098/rsta.2015.0202 (2016).
74. Pearson, K. L. I. I. I. on lines and planes of closest fit to systems of points in space. *The London, Edinburgh, and Dublin Philos. Mag. J. Sci.* **2**, 559–572. https://doi.org/10.1080/14786440109462720 (1901).
75. Hunter, R. F. H. aiirmap. github https://github.com/rfhhunter/aiirmap (2024).
76. Wes McKinney. Data Structures for Statistical Computing in Python. In Stéfan van der Walt & Jarrod Millman (eds.) Proceedings of the 9th Python in Science Conference, 56 – 61, https://doi.org/10.25080/Majora-92bf1922-00a (2010).
77. The pandas development team. pandas-dev/pandas: Pandas, version 2.2.2, https://doi.org/10.5281/zenodo.3509134 (Apr. 2024).
78. Helmers, H. et al. 68.9% efficient GaAs-based photonic power conversion enabled by photon recycling and optical resonance.. *physica status solidi (RRL) - Rapid Res. Lett.* **15**, 2100113. https://doi.org/10.1002/pssr.202100113 (2021).
79. Ayesha, S., Hanif, M. K. & Talib, R. Overview and comparative study of dimensionality reduction techniques for high dimensional data. *Inf. Fusion* **59**, 44–58. https://doi.org/10.1016/j.inffus.2020.01.005 (2020).
80. How, W. B., Wang, B., Chu, W., Tkatchenko, A. & Prezhdo, O. V. Significance of the chemical environment of an element in nonadiabatic molecular dynamics: Feature selection and dimensionality reduction with machine learning. *J. Phys. Chem. Lett.* **12**, 12026–12032. https://doi.org/10.1021/acs.jpclett.1c03469 (2021).

Acknowledgements

We acknowledge Dr. Daniel Poitras of the National Research Council of Canada for his help in generating the anti-reflection coating designs with simpler underlying epitaxial stacks. We also acknowledge CMC Microsystems for the provision of products and services that facilitated this research, including Synopsys Sentaurus TCAD.

Author contributions

R.F.H.H. built the optimization framework and conducted the simulations. G.P.F. built the calibrated optoelectronic Sentaurus model. D.P.W. provided the updated luminescent model, adapted from[64]. All authors contributed to the design of the experimental devices, which were grown by H.H., O.H., D.L., and C.P.. All authors contributed to the design of the study. Manuscript prepared by R.F.H.H. All authors reviewed the manuscript.

Funding

Funding provided by: Government of Canada's AI for Design National Research Council Collaborative Science, Technology, and Innovation Program under Grant INT-014-1. Government of Canada's National Research Council under Grant HSTN-645. National Sciences and Engineering Research Research Council of Canada

Discovery Research Program under Grant RGPIN-2022-03877. National Sciences and Engineering Research Research Council of Canada under Grant 497981. The Canadian Foundation for Innovation. The Government of Ontario. The German Federal Ministry of Education and Research under Grant 01DM21006A. ERC grant PHASE (No. 101125948).

Declarations

Competing interests

Karin Hinzer and Christopher E. Valdivia are president and chief technical officer of Enurgen Inc., respectively. The authors declare no other conflicts of interest.

Additional information

Supplementary Information The online version contains supplementary material available at https://doi.org/10.1038/s41598-025-16408-4.

Correspondence and requests for materials should be addressed to R.F.H.H.

Reprints and permissions information is available at www.nature.com/reprints.

Publisher's note Springer Nature remains neutral with regard to jurisdictional claims in published maps and institutional affiliations.

Open Access This article is licensed under a Creative Commons Attribution-NonCommercial-NoDerivatives 4.0 International License, which permits any non-commercial use, sharing, distribution and reproduction in any medium or format, as long as you give appropriate credit to the original author(s) and the source, provide a link to the Creative Commons licence, and indicate if you modified the licensed material. You do not have permission under this licence to share adapted material derived from this article or parts of it. The images or other third party material in this article are included in the article's Creative Commons licence, unless indicated otherwise in a credit line to the material. If material is not included in the article's Creative Commons licence and your intended use is not permitted by statutory regulation or exceeds the permitted use, you will need to obtain permission directly from the copyright holder. To view a copy of this licence, visit http://creativecommons.org/licenses/by-nc-nd/4.0/.

© The Author(s) 2025